Optics & Laser Technology 186 (2025) 112678

Contents lists available at ScienceDirect

Optics and Laser Technology

journal homepage: www.elsevier.com/locate/optlastec

Full length article

Laser-plume interactions in deep-penetration remote laser welding of stainless steel

Johannes Wahl [a,*], Christian Frey [b], John Powell [a], Felix Zaiß [a], Michael Haas [a], Simon Olschok [b], Uwe Reisgen [b], Christian Hagenlocher [a], Thomas Graf [a]

[a] Institut für Strahlwerkzeuge (IFSW), University of Stuttgart, Pfaffenwaldring 43, 70569 Stuttgart, Germany
[b] Institut für Schweißtechnik und Fügetechnik (ISF), RWTH Aachen, Pontstraße 49, 52062 Aachen, Germany

ARTICLE INFO

Keywords:
Laser welding
Welding fume
Vapor plume
Particle cloud
Thermal emission
Laser beam scattering

ABSTRACT

In deep-penetration laser welding a gaseous plume of metal vapor is ejected from the keyhole. Cooling of this vapor then leads to condensation and the formation of a particle cloud above and around the welding zone. The vapor plume and particle cloud interact with the incident laser beam by scattering, absorption, and deformation of the phase front. This complex and dynamic interaction can have detrimental effects on the welding result and is not yet fully understood. This is particularly relevant for welding applications where the vapor plume is not removed with shielding gas or a cross-jet. The present paper reports on investigations into the beam-plume interactions by analyzing the thermal emission and scattered laser light from the interaction zone while welding stainless steel. A high-speed camera with optical filters and a spectrometer were used for this analysis. In addition, Schlieren and shadow images were recorded to visualize the beam-plume interaction. Different zones of beam-plume interaction were distinguished. Near the laser beam focus, a negligible amount of condensed or solid material scattering the laser beam was found within the laser beam caustic. Instead, the thermal emission of the hot metal vapor was found to be the main source of emission in this area. At greater distances from the focus, the scattered laser light was the dominant emission source, while the thermal emission became negligible. These two zones were found to be connected by a multi-phase zone, which could be observed by its thermal emission and the scattering of the laser light, which contained both hot metal vapor and particles. The investigations presented here provide valuable insights into the interactions between the vapor plume and the particle cloud. In the future, this knowledge can be used to avoid or compensate for related adverse effects that occur during laser deep penetration welding, and as a basis for simulations of the beam-plume interaction.

1. Introduction

Deep-penetration laser welding is a well-established industrial process. As the welding capillary (keyhole) forms, a small fraction of the material is evaporated. A proportion of this vapor is emitted from the keyhole [1], and can interact with the incident laser beam. In the context of high-power CO_2 laser welding, the vaporized metal undergoes heating until it transforms into a plasma, as evidenced by Miyamoto et al [2]. However, in solid-state laser welding, the gaseous metal vapor exhibits much reduced absorption of the processing laser beam, resulting in the formation of a weakly ionized plume [2,3]. Generally, as the vapor cools, it generates a cloud of small particles. Both the size and density of the particles within the cloud have been investigated by Shcheglov et al [4]. The vapor plume and particle cloud interact with the incident laser beam through scattering and absorption mechanisms and can be described by the Mie theory [5,6]. This is particularly relevant for welding applications where shielding gas or cross-jets cannot fully remove the vapor plume. In remote welding, where the laser optics might be over a meter away from the weld zone, cross-jets primarily protect laser optics from spatter but often fail to clear the plume from most of the beam path. The significance of cross-jet positioning for effective plume removal is discussed in [7,8].

Gradients of the refractive index above the welding zone, which are either induced by the hot metal vapor or the heated air, also play a part

* Corresponding author.
E-mail addresses: johannes.wahl@ifsw.uni-stuttgart.de (J. Wahl), christian.frey@isf.rwth-aachen.de (C. Frey), dr_johnpowell@yahoo.co.uk (J. Powell), felix.zaiss@ifsw.uni-stuttgart.de (F. Zaiß), michael.haas@ifsw.uni-stuttgart.de (M. Haas), olschok@isf.rwth-aachen.de (S. Olschok), office@isf.rwth-aachen.de (U. Reisgen), christian.hagenlocher@ifsw.uni-stuttgart.de (C. Hagenlocher), thomas.graf@ifsw.uni-stuttgart.de (T. Graf).

https://doi.org/10.1016/j.optlastec.2025.112678
Received 12 August 2024; Received in revised form 7 January 2025; Accepted 20 February 2025
Available online 28 February 2025
0030-3992/© 2025 The Author(s). Published by Elsevier Ltd. This is an open access article under the CC BY license (http://creativecommons.org/licenses/by/4.0/).

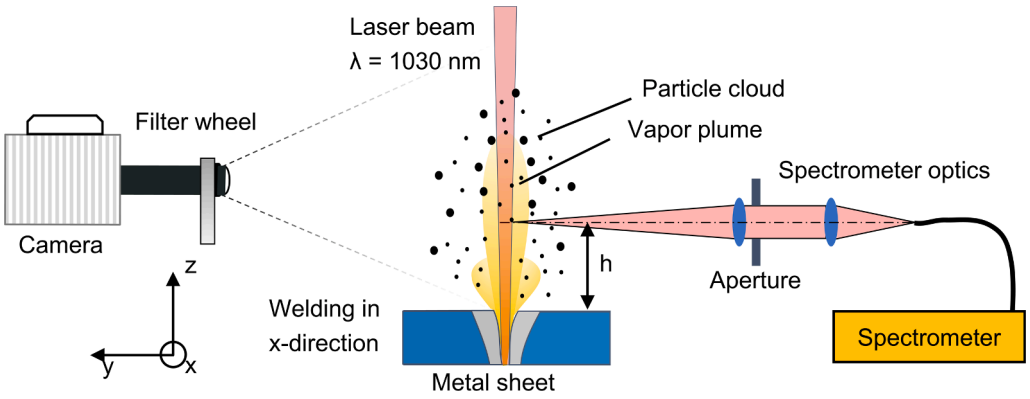


Fig. 1. Schematic of the experimental set-up for the analysis of the thermal emission of the vapor plume and the scattering of the laser beam by the particle cloud during full-penetration welding of stainless steel. The set-up utilizes a high-speed camera combined with a filter wheel that has three configurations: No optical filter, a short pass filter ($\lambda_{SP} < 950$ nm) and a band pass filter ($\lambda_{BP} = 1030 \pm 5$ nm). In addition, a spectrometer is used for spectrally resolved measurement at different distances h along the beam axis.

in the beam-plume interactions. These gradients lead to phase front aberrations, consequently leading to changes in the distribution of the irradiance on the workpiece. This is of particular importance for beam shaping technologies that are based on interference patterns, and therefore require a highly stable and unperturbed propagation of the beam to achieve the desired irradiance profile on the workpiece.

The effect of refractive index gradients on the phase front of a laser beam has been explained by Born et al [9]. Brignon [10] later suggested the idea of using coherent beam combining to compensate for atmospheric turbulence. Current techniques use coherent beam combining to achieve near diffraction limited high-power laser beams [11]. Regardless of the application, knowledge of refractive index gradients along the optical path is therefore essential.

A numerical model and simulation of the fluctuating lower vapor plume and its effect on the keyhole dynamics was created by Yang et al [12]. Together with the numerical simulation of Pang et al [13], which focussed on the vapor dynamics in the keyhole, this work shows the interdependence between the evaporation in the keyhole and the influence of the ejected vapor on the laser beam. Kurita et al [14] experimentally investigated the interdependence between the emission of the vapor plume and the corresponding keyhole instability.

To properly address the challenges that arise from the beam-plume interactions, a more profound knowledge of these interaction mechanisms is required. Previous efforts have generally concentrated on the overall properties of the vapor plume and the particle cloud. For instance, [4,5,15] examined the particle size and the resulting attenuation of the laser beam. Uspenskiy et al [16], introduced an additional coaxial probe laser beam to qualitatively show scattering within the particle cloud, and also measured the temperature of the plume. In their work, they stated that in the lower part of the plume, weakly ionized metal dominates the emission, while in the upper plume the emission originates from heated particles.

The present work builds on the ideas of Uspenskiy et al [16] and investigates the local thermal emission and scattering characteristics throughout the laser beam caustic. This approach allows us to look into the beam-plume interaction zone and draw conclusions about the properties of the vapor plume and particle cloud. The knowledge gained about the local beam-plume interaction can help us to understand the causes of, and thus avoid, related detrimental effects on the welding result.

Initially, shadow imaging was implemented to gain information about the particle cloud in general. Secondly, a high-speed Schlieren imaging set-up was employed to qualitatively show the effect of induced refractive index gradients onto the phase front of the laser beam. Finally, high-speed imaging with different optical filters was used together with a spectrometer to capture the thermal emission and scattered laser light. This combination of instruments enabled high spatial as well as high spectral resolution. This gave qualitative insights into the behavior, temperature, and composition of the vapor plume and particle cloud, with particular focus on the beam-plume interactions.

2. Experimental set-up

The experimental set-up used for capturing the thermal emission and the scattered laser radiation from the vapor plume and particle cloud is shown in Fig. 1. Sheets of 4 mm thick stainless steel (1.4301) were

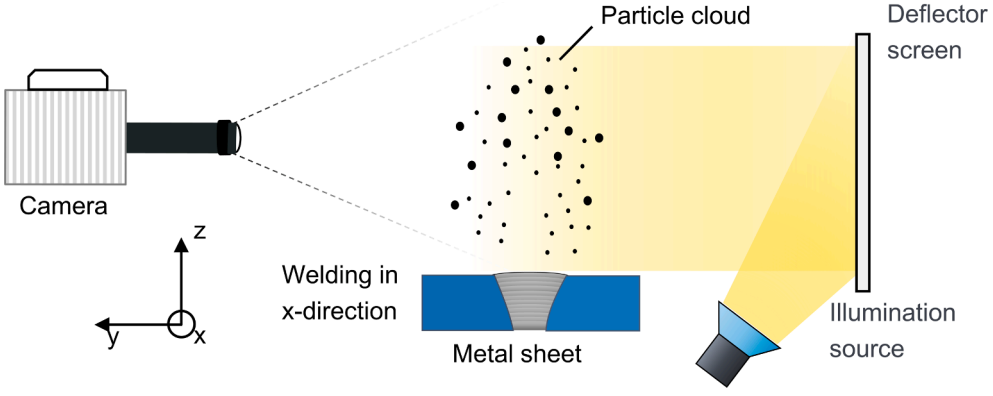


Fig. 2. Schematic of the experimental set-up for high-speed shadow imaging of the particle cloud/welding plume during full-penetration welding of stainless steel. P = 5.5 kW, v = 2 m/min. Background illumination is used to visualize the particle cloud after the welding process is completed.

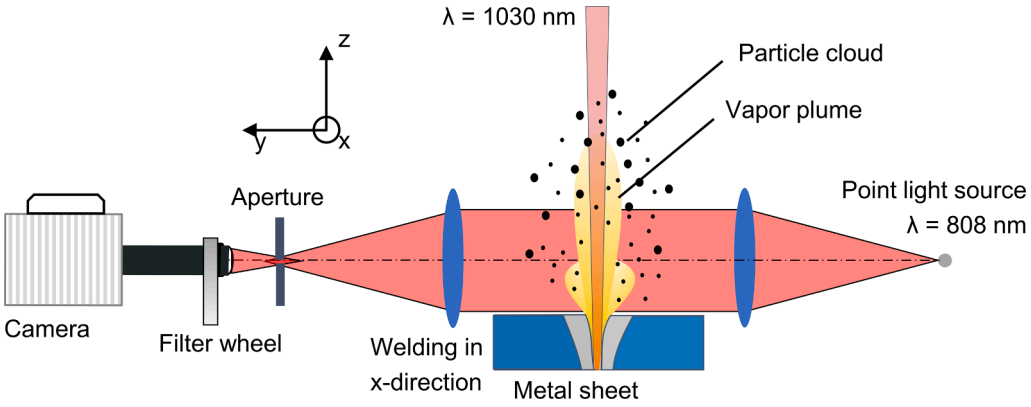


Fig. 3. Schematic experimental setup of the Schlieren imaging for the visualization of the gradients of the refractive index in the metal vapor and hot air above the workpiece during full-penetration laser welding of stainless steel. P = 5.5 kW, v = 2 m/min.

welded using a fiber-coupled TruDisk 16,002 laser at a wavelength of $\lambda = 1030$ nm. The core diameter of the fiber was 400 µm. Using focal lengths of $f_{coll} = 150$ mm for collimation and $f_{focus} = 400$ mm for focusing, led to a focus diameter of 1.07 mm on the surface of the sample. Full-penetration welding was achieved with a laser power of 5.5 kW and a feed rate of 2 m/min. The processing beam was inclined at an angle of 5° from the perpendicular (dragging) to the sheet surface.

As illustrated in Fig. 1, a high-speed camera was used to capture a view of the entire welding plume. The camera was positioned 2.2 m from the plume and equipped with a 70 mm focal length objective lens. An exposure time of 20 µs, combined with an aperture setting of f/11, provided an optimal balance between depth of field and image brightness. The frame rate of the IDT OS8 camera was set to 8000 Hz. The high-speed videos were recorded in three ways: without an optical filter, with a shortpass filter ($\lambda_{SP} < 950$ nm) and with a bandpass filter ($\lambda_{BP} = 1030 \pm 5$ nm). Additionally, a fiber-coupled OceanOptics 4000 spectrometer with a fiber core diameter of 200 µm was used. Combined with a 50 mm collimation and 300 mm focusing lens this resulted in a measurement spot diameter of 1200 µm. An iris aperture was added to the spectrometer's collimation optics in order to minimise overexposure. As depicted in Fig. 1, the spectrometer's measurement spot coincided with the processing beam axis and was horizontally aligned at various heights above the workpiece. The combination of an aperture in the beam path and the fiber connected to the spectrometer ensures that no off-axis light is detected, making the measurement robust against stray light or reflected laser light from the keyhole. The acquisition rate of the spectrometer was 100 Hz with an integration time of 3.8 ms for each individual spectrum.

High-speed shadow imaging of the particle cloud was conducted using the experimental arrangement described in Fig. 2. To capture a clear image of the particle cloud, an exposure time of 1000 µs and an aperture setting of f/5.6 were used. For this purpose, a diffuse deflector positioned opposite the camera was illuminated with a spotlight, which served as background lighting for the particle cloud.

The refractive index gradients within the plume were visualized using a Schlieren imaging setup [17]. Schlieren imaging is an optical method of observing refractive index gradients within fluids. These gradients can result from variations in temperature, pressure, density, or the presence of gases with differing optical properties. A lens-based, linear arrangement was employed for this setup, as depicted in Fig. 3. The fiber output of a Cavitar Cavilux HF illumination laser with a wavelength of $\lambda = 808$ nm was used as a point light source. Both the collimation and focusing lenses had a focal length of 600 mm and a diameter of 150 mm. An iris aperture was positioned in the Fourier plane of the focusing lens to obtain the Schlieren image. A bandpass filter with a central wavelength of $\lambda_{BP} = 808$ nm was placed in front of the camera. The frame rate of the IDT OS8 camera was, once again, set at 8000 Hz.

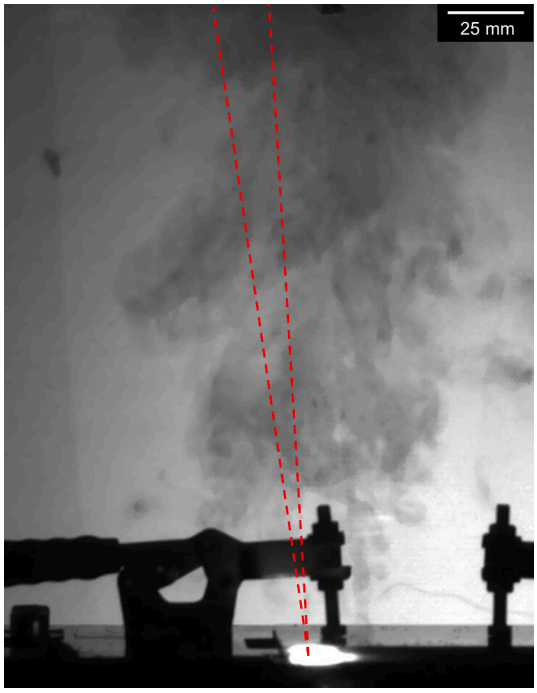


Fig. 4. Shadow image taken with the set-up from Fig. 2 of the particle cloud illuminated with a diffuse deflector 10 ms after the end of the welding process. The particle cloud appears as a diffuse dark cloud covering the entire beam propagation distance from the welding optics to the weld zone, with the red dashed line indicating the approximate position of the laser beam.

3. Results

3.1. Shadow imaging

Fig. 4 shows a single frame of the shadow imaging of the welding plume. This image was captured approximately 10 ms after the welding process ended to exclude the interaction of the laser beam with the plume. Against the illuminated background it is clear that, during laser welding, a particle cloud extends over the entire distance from the metal sheet to the laser optics. During welding this particle cloud is accompanied by hot gaseous metal vapor. Both the particle cloud and the vapor interact with the laser beam in ways which will be discussed in the following sections.

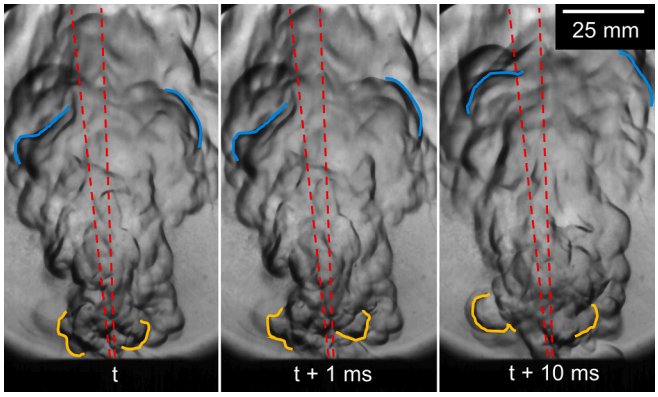


Fig. 5. Single frames of high-speed Schlieren imaging of the vapor plume at different time steps using the set-up from Fig. 3. The orange lines show the rapid changes in the refractive index in the lower cloud, while the blue lines show the slower changes in the upper cloud. The video file is available at [18].

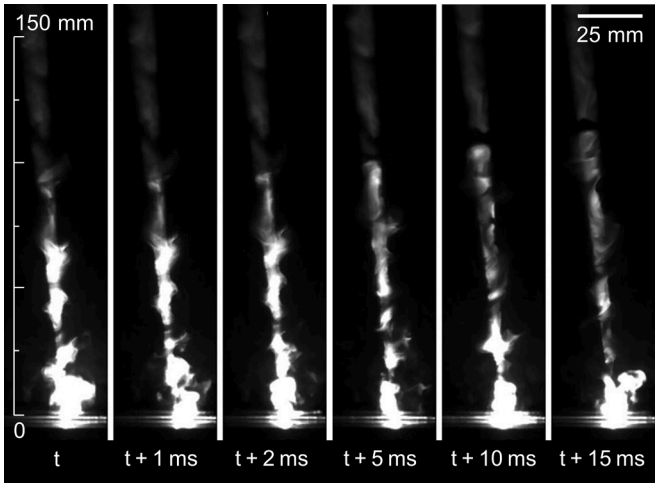


Fig. 6. Single images of the vapor plume at different time steps during full-penetration laser welding of stainless steel. No optical filter was used, allowing the observation of both thermal emission and scattered laser light. The red dashed line shows the approximate beam caustic. The video file is available at [18].

3.2. Schlieren imaging

Fig. 5 presents three frames at different time steps from the Schlieren high-speed recordings described in Fig. 3. Schlieren photography enables the visualization of gradients of the refractive index transverse to the optical path. The contrast variations in the images are a result of a deflection of the light from its original path. Whether the gradients of the refractive index have their origin in temperature gradients in the air or in local variations of the density of the metal vapor cannot be determined from the Schlieren images. However, it is clear that the local refractive index changes rapidly throughout the plume. The time scales of these fluctuations can be estimated from the images and, in order to visualize the temporal behavior of the plume, some features in the Schlieren images have been marked to guide the eye. In Fig. 5, the orange markings in the plume close to the welding zone show very rapid changes (within 1 ms). In comparison, the blue markings in the upper plume indicate slower fluctuations and movements.

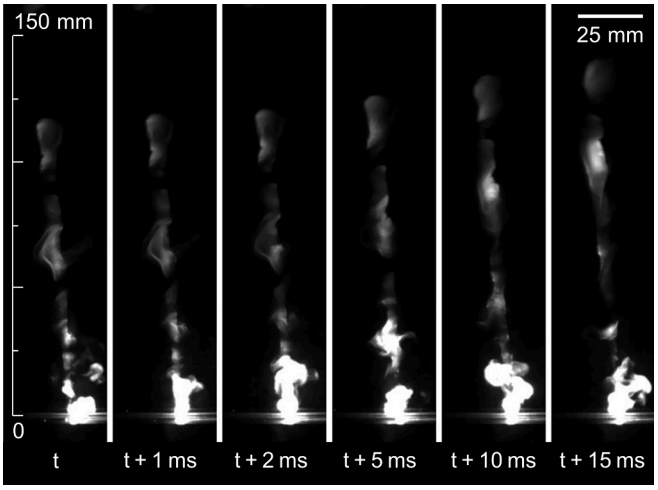


Fig. 7. Single images of the vapor plume at different time steps during full-penetration welding of stainless steel recorded through a shortpass filter $\lambda_{SP} < 950$ nm (thermal emission). The red dashed line shows the beam position. The video file is available at [18].

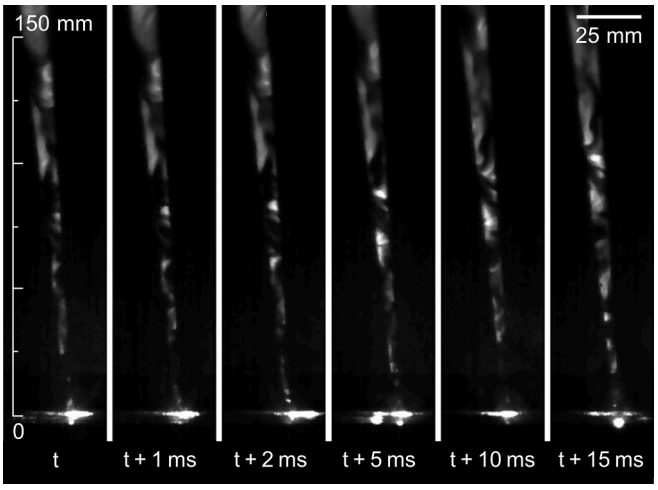


Fig. 8. Single images of the vapor plume at different time steps during full-penetration welding of stainless steel recorded through a bandpass filter $\lambda_{BP} = 1030 \pm 5$ nm (scattered laser radiation). The red dashed line shows the beam position. The video file is available at [18].

3.3. Filtered imaging of the thermal and scattered laser emissions from the plume

The high-speed imaging set-up used to capture the thermal emission and the laser radiation scattered from the plume enabled both high temporal resolution and a large field of view. As depicted in Fig. 1, the videos were recorded using different optical filters.

Images of the vapor plume, recorded without an optical filter can be seen in Fig. 6. These images show both thermal emission and scattered laser light simultaneously, due to the broad spectral sensitivity of the camera from about 200 nm to 1100 nm, which includes all the visible spectrum and the laser wavelength of 1030 nm.

Fig. 7 shows images obtained by recording through the shortpass filter with $\lambda_{SP} < 950$ nm. As the laser wavelength of $\lambda = 1030$ nm is well above the filter cut-off, it is therefore attenuated by roughly five orders of magnitude, according to the datasheet provided by the filter manufacturer. This ensures that the images capture only thermal emission,

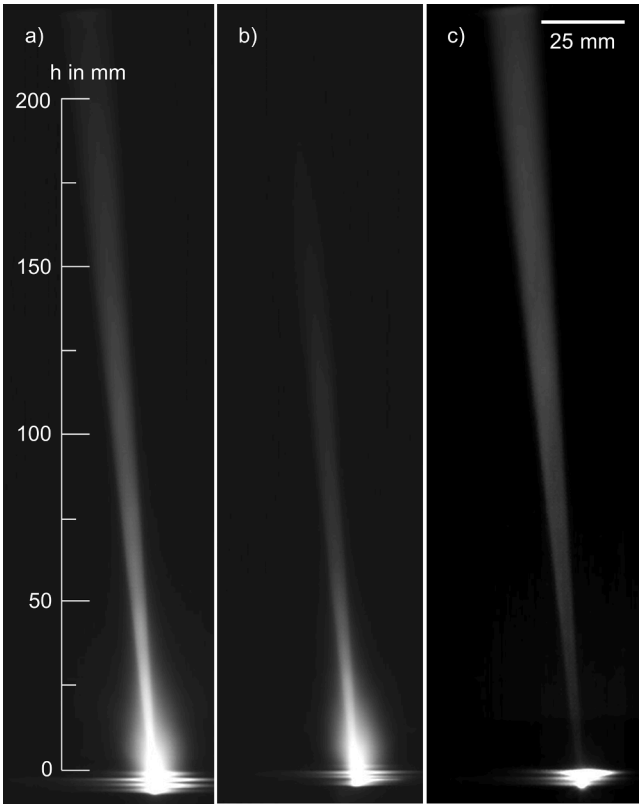


Fig. 9. Average images of the vapor plume created from 8000 frames over 1 s during full-penetration laser welding of stainless steel with different filter settings: a) without filter, b) with a shortpass filter $\lambda_{SP} < 950$ nm (thermal emission) and c) with a bandpass filter $\lambda_{BP} = 1030 \pm 5$ nm (scattered laser radiation). The video file is available at [18].

which includes both broadband Planck emission and thermally induced atomic line emissions. In contrast, the images shown in Fig. 8 only show the scattered laser light, as a result of the narrow bandwidth of $\Delta\lambda = 10$ nm of the bandpass filter, centred at $\lambda_{BP} = 1030$ nm. This narrow bandwidth does not allow enough thermal radiation to pass to become visible in these images at the given exposure configuration of the camera. This can be clearly seen in Fig. 8, where the scattered laser emission is strictly bound to the volume of the laser beam caustic, in contrast to the thermal emission in Fig. 7. It should be mentioned that the pictures shown in the Fig. 6 through Fig. 8 were not recorded simultaneously and therefore do not show exactly the same plumes.

In agreement with the Schlieren results presented in Fig. 5, it is clear from Fig. 6 and Fig. 7 that the vapor plume is extremely dynamic, particularly in the lower areas, close to the welding zone. On occasion, the thermal emission images depicted in Fig. 7 exhibit some clusters of material that either diminish or intensify in brightness. For instance, between t and t + 2 ms the thermal emission of the cluster spanning the height between 50 mm to 75 mm and the one at a height of about 25 mm decreases, suggesting material that cools as it exits the laser beam. In the subsequent timesteps from t + 5 ms to t + 15 ms, the thermal emission of the cluster moving up from 75 mm to 100 mm increases, indicating a re-heating of material that re-enters the laser beam caustic.

3.4. Average images of plume emissions

Due to the rapid fluctuations of the vapor plume and particle cloud, average images were created from the high-speed recordings for further evaluation. For this purpose, 8000 frames, which correspond to a time period of 1 s, were taken after the welding process reached its steady

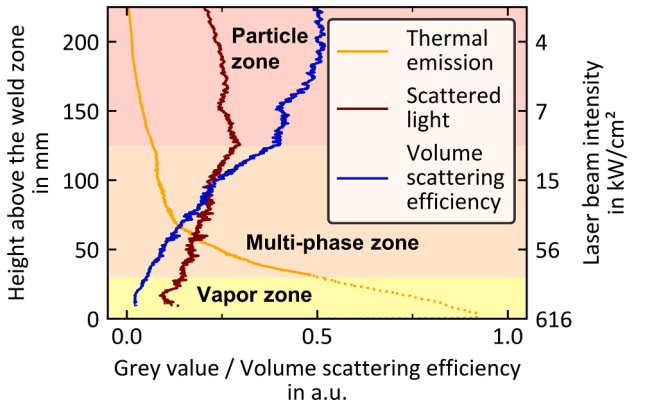


Fig. 10. Grey values of the average images from Fig. 9 along the laser beam axis. a) The orange line results from the image with a short pass filter $\lambda_{SP} = 950$ nm and corresponds to thermal emission. b) The red line GV_{sca} results from the image with a bandpass filter $\lambda_{BP} = 1030/10$ nm and corresponds to scattered laser light. c) The blue line $Q_{vol,sca}$ results from the grey values GV_{sca} of b) corrected for local beam diameter and laser intensity and corresponds to the dimensionless volume scattering efficiency. Zone labels for the respective regions are explained in Section 4.

state. The averaged images recorded through the different filters are displayed in Fig. 9: Fig. 9a was taken without a filter, Fig. 9b with the shortpass filter $\lambda_{SP} < 950$ nm, and Fig. 9c with the bandpass filter at $\lambda_{BP} = 1030 \pm 5$ nm. Therefore, as described above, Fig. 9b shows thermal emission, Fig. 9c shows scattered laser light and Fig. 9a shows both. Despite the rapid local fluctuations of the plume, these images appear smooth after the temporal averaging. The lower part of the plume, up to approximately 50 mm, appears very similar in Fig. 9a and Fig. 9b, where the scattering contribution to the image brightness is low. In contrast, the upper part is dominated by scattered light, as indicated by the increasing grey values with distance from the keyhole, as shown in Fig. 9c.

To further evaluate the averaged images, the grey values along the axis of the laser beam in Fig. 9b and Fig. 9c are plotted in Fig. 10. The orange line corresponds to the thermal emission along the beam axis in Fig. 9b and indicates a steady temperature decrease with increasing distance from the keyhole and thus the laser beam focus. The grey values of the dotted orange line below a height of 30 mm should be treated with caution, as some of the frames contributing to the average image are overexposed in this area. Taking this into account, even higher grey values could be expected in this zone.

The red line represents the grey values (GV_{sca}) along the beam axis in Fig. 9c, corresponding to the scattered laser light along this axis. Each pixel captures the emission from a small, elongated volume traversing the width of the laser beam caustic. Thus, the brightness of one illuminated pixel in the image is directly influenced by the beam diameter. Furthermore, as is known from the Mie theory, see [19], the scattering intensity, which is proportional to the resulting grey value (I_{sca} GV_{sca}), is linearly dependant on the local laser beam intensity (I_{beam}). To determine the local volume scattering efficiency ($Q_{vol,sca}$) of the particle cloud within the laser beam caustic, the grey values for scattered light were adjusted, to take into account the beam diameter and local laser beam intensity:

$$Q_{vol,sca} = \frac{GV_{sca}}{d_{beam} \bullet I_{beam}} \quad (1)$$

This calculation assumes a top-hat beam profile. The calculated volume scattering efficiency, $Q_{vol,sca}$, is shown as a blue line in Fig. 10. This dimensionless parameter essentially represents the scattering strength of a normalized volume within the laser beam caustic. Assuming a uniform particle size distribution and a constant complex refractive index along the beam axis, the volume scattering efficiency is an effective measure of

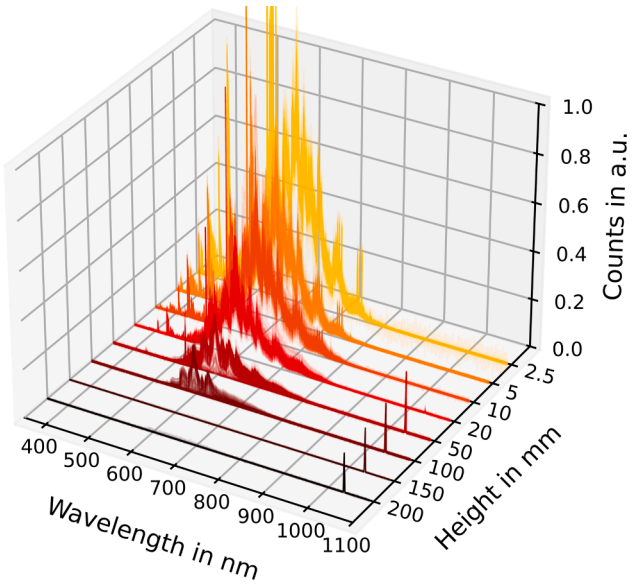


Fig. 11. Captured raw spectra along the beam axis from the vapor plume and particle cloud at different heights above the keyhole. The relative intensities between the plots are not to scale and have been adapted for better visibility. 2D plots of the spectra for each height are given in the Appendix B: Spectrometer measurements. The spectra data files are available at [18].

particle density.

3.5. Spectrometer measurements

Fig. 11 presents the raw spectra of the emission measured at different heights above the keyhole (and thus the laser beam focus). Spectra below or above a certain threshold have been removed, to filter the data for under- or over-exposure. In order to reduce overexposure during the measurement in the first place, the iris aperture shown in Fig. 1 was adapted for each height h. Therefore, the relative intensities of the spectra are not to scale. However, the captured raw spectra are useful for qualitative evaluation. For example, the spectra from 2.5 mm up to 20 mm show distinct atomic line emissions, which indicate very high temperatures.

Spectra less than 20 mm from the opening of the vapor keyhole show almost no scattered light at the laser wavelength of $\lambda = 1030$ nm. This indicates the absence of particles in the plume in this area. In general, atomic line emission occurs around the evaporation temperature and above as described in [20]. The amount and intensity of atomic lines gives insights into the temperature of the gaseous metal, as described in [21]. The spectra at a height of 50 mm and 100 mm above the weld zone (beam focus) show greatly reduced atomic line emission, therefore indicating a lower temperature which correlates well with the grey values of the thermal emission (orange line) in Fig. 10. The spectra recorded at the heights of 150 mm and 200 mm feature negligible thermal emission, but a distinct peak of scattered laser light at $\lambda = 1030$ nm.

4. Discussion

In the following, three zones within the interaction volume of the laser beam and the vapor plume/particle cloud are defined. These zones are distinguished by characteristic thermal and scattered laser emission that correspond to their physical properties and interaction mechanisms with the laser beam.

4.1. Vapor zone

Reviewing the high-speed videos, from which the sequences shown in Fig. 7 and Fig. 8 were taken, as well as the spectra in Fig. 11, several observations can be made about the zone closest to the laser focus, just above the welding area:

i. Hot material, presumably weakly ionized gaseous metal vapor [3], is ejected from the welding keyhole as a rapidly fluctuating plume up to approximately 35 mm high, at the welding parameters used here (see Fig. 7 and Fig. 9b).
ii. The intensity of scattered laser light at $\lambda = 1030$ nm is extremely low below a height of approximately 35 mm from the opening of the keyhole (see Fig. 8, Fig. 9c and Fig. 10). This indicates that there is a negligible amount of particles within the beam caustic in this area.
iii. Up to 50 mm above the opening of the keyhole, the number of atomic lines and their intensities in the spectra decreases, indicating a reduction in temperatures within the plume (see Fig. 11).

The ejection of vapor from the keyhole creates a volume of hot material which is clearly visible from its thermal emission, as shown in Fig. 9b. The zone within this volume, which contains hot gaseous metal vapor and a negligible number of scattering particles, can be referred to as the *vapor zone*. The small amount of scattering particles in this zone can be explained by the generally high temperature in this area and, within the beam caustic, due to the high laser beam intensity in the vicinity of the focus. The latter prevents vapor from condensing into particles and causes any particles that may enter this zone, even at greater distances from the keyhole opening, to evaporate rapidly. In this specific welding configuration, the vapor zone within the beam caustic extends over approximately 35 mm in the axial direction above the weld (and beam focus). Hot vapor from the capillary also extends laterally, beyond the narrow area of the beam caustic. This is clear from the width of the thermal emission signal in the area just above the weld zone. This laterally expanding hot vapor will cool rapidly in the surrounding air.

Due to the low absorption of laser radiation (at a wavelength of around 1 μm) in the iron vapor, it can be assumed that the vapor can momentarily condense within the laser beam caustic, even near the focus [3]. However, as soon as condensation sets in and droplets form, greater absorption and thus re-heating and possible re-evaporation can be expected. Once a sufficient distance from the weld is reached, and the laser intensity is low enough, droplets can condense without necessarily being re-evaporated, as discussed in the next section.

4.2. Multi-phase zone

As the ejected vapor spreads laterally and cools down, it is no longer visible in the thermal emission image (Fig. 9b). During cooling, the vapor condenses and then solidifies into particles, giving off the corresponding latent heat. Additionally, the particles or droplets oxidize during the cooling process, generating additional heat due to the exothermic oxidation reactions involved. Rapid and complete oxidation of the gaseous metal and associated nano-particles can be assumed, due to thermodynamic considerations and the very large surface-to-volume ratios involved [5,22,23].

Above the vapor zone (in this case starting from roughly 35 mm) we can define a *multi-phase zone*, in which hot material generates thermal emission, but only in the immediate vicinity of, and within, the laser beam. Additionally, scattered laser light becomes more significant in this zone. From the results presented above, several statements can be made about the multi-phase zone:

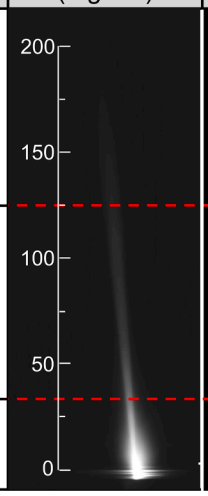
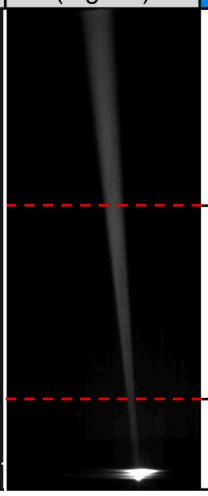
	Approximate height (for used configuration)	Thermal emission (Fig. 9b)	Scattered laser light (Fig. 9c)	Dominant source of emission	Material within the beam
Particle zone	h > 125 mm			Scattered laser light	Solid (and liquid) particles
Multi-phase zone	35 mm < h < 125 mm			Scattered laser light and thermal emission	Gaseous vapor, liquid and solid particles
Vapor zone	h < 35 mm			Thermal emission	Gaseous vapor

Fig. 12. Tabular description of the different zones in the metal vapor plume during deep penetration laser welding of stainless steel.

i. From the thermal emission visible in Fig. 7, it is clear that there is evidence of hot metal vapor and/or hot particles at a height greater than 35 mm above the weld (i.e. above the vapor zone).
ii. Over several milliseconds, some areas that were previously dark increase in brightness, which indicates the re-heating of air-borne material which has drifted into the path of the laser beam (see thermal emission in Fig. 7).
iii. Both the images in Fig. 8 and Fig. 9c, as well as the spectra in Fig. 11 clearly show scattered laser light above a height of approximately 35 mm from the opening of the keyhole, which implies the presence of either liquid or solid particles within the beam caustic.

These observations indicate the existence of hot particles, droplets and metal vapor within the laser beam caustic in the multi-phase zone. Based on the decreasing grey values of the thermal emission (orange line) in Fig. 10, the average thermal emission (and therefore the temperature) of the re-heated material decreases steadily as it gets further away from the opening of the keyhole (and the laser beam focus). At the same time, the volume scattering efficiency (blue line) increases throughout the multi-phase zone, indicating an increase in the number of particles that scatter the laser beam.

It is probable that the multi-phase zone contains hot material from two sources:

i. Vapor/metal gas or particles from the vapor zone which has remained hot within the laser beam.
ii. Vapor or particles, which come from material that has cooled down outside the beam, condensed into droplets, oxidised and solidified but has been re-heated upon re-entering the beam.

The re-heating of material that re-enters the beam might result in reduction (de-oxidation), melting and even re-evaporation. At this point, it should be noted that the average images in Fig. 9 and the corresponding line graphs in Fig. 10 provide an insight into trends, but do not describe the specific behavior of individual particles. That said, it is assumed that the rate of heating and likelihood of rapid evaporation for a single particle that re-enters the laser beam increases with the local laser intensity (which increases with decreasing distance from the laser beam focus).

Both the grey values of the scattered light (red line) and the volume scattering efficiency (blue line) in Fig. 10 feature a kink at a height of about 125 mm above the opening of the keyhole. This marks the approximate upper limit of the multi-phase zone and the start of the particle zone.

4.3. *Particle zone*

Above the multi-phase zone, within which particles may be re-heated up to evaporation, we can observe a cooler zone within the laser beam, which we can refer to as the *particle zone*. Within this zone we can observe:

i. The absence of atomic line emissions in the spectra at heights exceeding 150 mm (see Fig. 11) indicates that there is no hot, gaseous vapor present above this height.
ii. The thermal emission in the particle zone decreases even further with increasing height above the welding zone and becomes negligible compared to the emission of scattered laser light (see Fig. 9 and Fig. 11).
iii. The volume scattering efficiency no longer exhibits the same rate of increase as in the multi-phase zone. Instead, it flattens out to a plateau level (see Fig. 10).

Within this particle zone the laser intensity is too low to evaporate particles during re-heating, although they may be melted or reduced (de-oxidised). Based on the previous assumption of constant particle size and chemistry and a top-hat intensity distribution, the plateau of the volume scattering efficiency can be explained by a stagnating particle density in the particle zone. For a more precise analysis of the laser light scattered by the (oxidised) particles, it would be necessary to delve deeper into the scattering behavior of these particles. The chemical and thus optical properties of the particles significantly influence the complex refractive index and thus the scattering behavior. If the size and complex refractive index of the particles are known, their scattering and absorption behavior can be calculated using the Mie theory [19]. Apart from the differences in optical properties between oxides and their metals, it is worth noting that oxidised particles will be larger and heavier than their un-oxidized counterparts.

By extending the rationale based on the re-heating and melting of particles within the particle zone, one can postulate the existence of an upper, sub-zone where the melting point is not reached during the re-

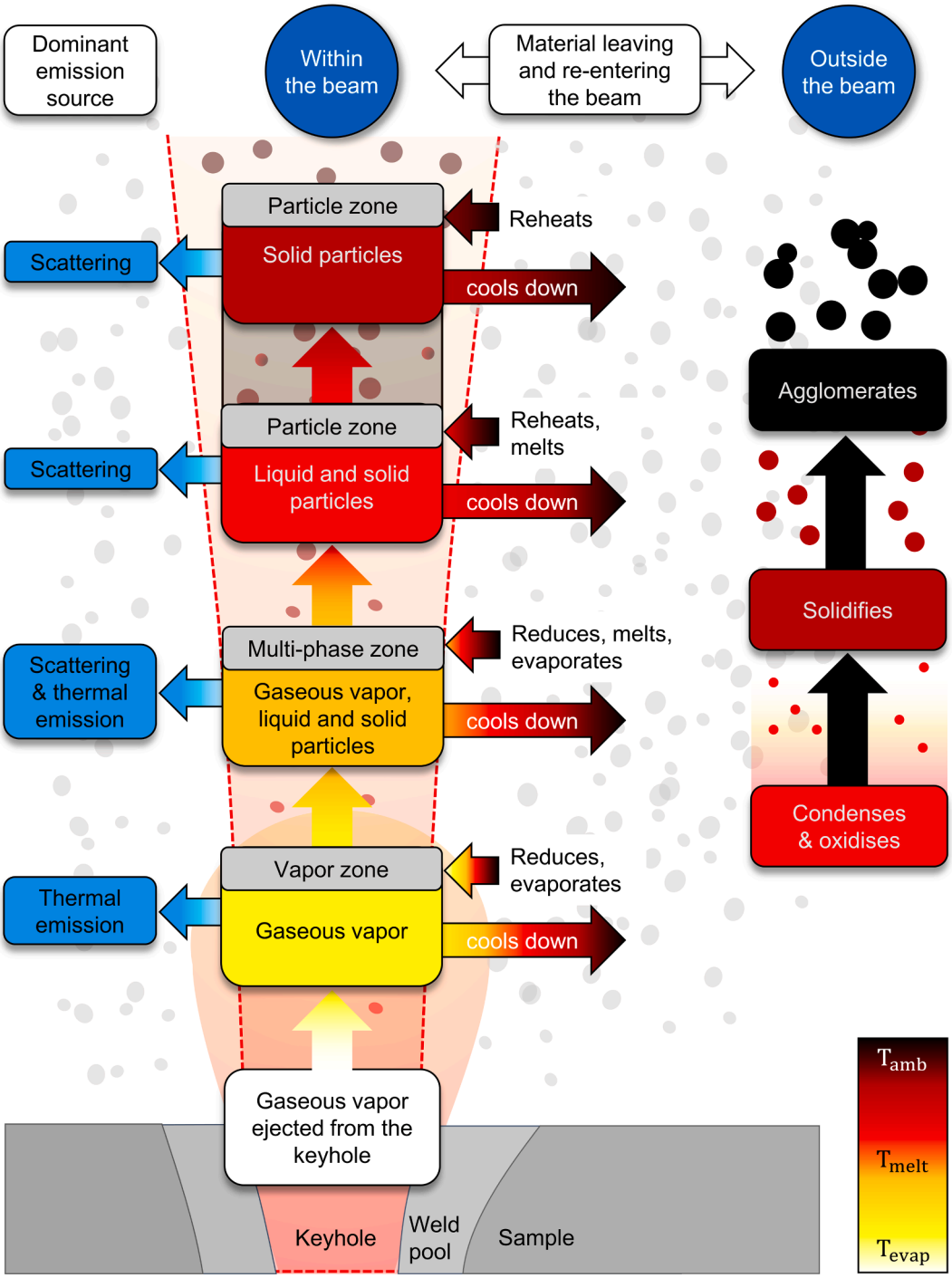


Fig. 13. Schematic visualization and description of the different zones in the metal vapor plume during deep-penetration laser welding of stainless steel.

heating process. Within this solid particle zone, there would be neither vapor nor liquid metal present.

The results presented here indicate changes of the properties and behavior of the vapor plume and particle cloud due to the high laser intensities within the laser beam caustic in laser welding. Although the vapor plume and particle cloud undergo rapid dynamic fluctuations, as can be seen from Fig. 6, Fig. 7 and Fig. 8, their average properties in any area are rather stable, as seen in Fig. 9 and Fig. 10. From the results presented in this work, the existence of three laser-plume interaction zones can be derived. Moving away from the laser opening of the keyhole, a vapor zone, a multi-phase zone and a particle zone form. A short tabular description of the zones is given in Fig. 12.

Due to the pressure gradient from the keyhole opening to the atmosphere above, gaseous metal vapor is emitted from the keyhole opening [24]. Most of this gaseous vapor exits the laser beam caustic in the vapor zone and will cool down rapidly, condensing and oxidising as it cools [5,22,23]. Eventually a particle cloud is formed in the area around the welding process, see Fig. 4.

Both the condensation and oxidation contribute to the heating of the surrounding air. Local thermal gradients, together with the presence of gaseous metal itself, lead to refractive index gradients in the laser beam path. A visualization of the effect of these refractive index gradients on the phase front of a propagating beam, can be seen in the Schlieren imaging in Fig. 5.

Within the particle cloud, the particles agglomerate in sizes in between roughly 2——200 nm [5,25–27]. However, it was observed during this work that a proportion of the solidified particles drifted back into the beam caustic.

If the particles re-enter the laser beam caustic in the vapor zone, they are likely to be rapidly evaporated by the high intensity laser beam near the focal point. Both the high grey values of the average image of thermal emission below approximately 35 mm, shown in Fig. 9b, as well as the spectra for the corresponding height in Fig. 11, suggest very high temperatures within the laser beam in the vapor zone. The low grey values below approximately 35 mm in the average image for scattered light in Fig. 9c and the corresponding spectra also suggest that almost no particles or droplets are present in the vapor zone.

If particles re-enter the laser beam caustic in the multi-phase zone (between approximately 35 to 125 mm with the used welding parameters) they will be re-heated by the interaction with the laser radiation. The level of re-heating is influenced by the local intensity of the laser beam, the particle chemistry and the particle size. The particles may or may not reach evaporation temperature and/or be reduced (de-oxidised). Moving up, away from the focus, the plume exhibits an increasing dimensionless volume scattering efficiency and a simultaneous decrease in thermal emission, as shown in Fig. 10. This indicates an increasing number of particles that scatter laser light and a decreasing average temperature.

In the particle zone (above approximately 125 mm with these welding parameters), particles are re-heated to below the evaporation temperature. They therefore continue to absorb and scatter the laser beam, as can be seen in Fig. 9c, Fig. 10 and Fig. 11.

Fig. 13 presents a flow chart of the interactions between the ejected vapor and the laser beam. It also describes the changes in state that the material undergoes within and outside the laser beam after it is ejected from the keyhole.

It is assumed that similar zones (at different heights) form in any deep-penetration laser welding process, as long as the process plume is not removed. The quasi-equilibrium that leads to the formation of zones within the laser caustic is governed by complex thermodynamic processes. These processes include cooling by radiative and convective heat loss, reheating by absorption of incident laser radiation, and heating by oxidation. The overall dynamics depend on the physical form, thermophysical and optical properties of the material. Therefore, the occurrence of these zones depends, among other things, on the local laser intensity, the material being welded, and the ambient atmosphere (including pressure and oxygen content), which are key parameters of the processes described above. The existence and local extent of the zones using other welding parameters and other materials can be verified using the same methodology and will be the subject of future research.

5. Conclusions

In this investigation, the complex interactions between a high-power laser beam and the gaseous metal vapor plume generated during deep-penetration laser welding were thoroughly examined. The following conclusions can be derived from the work presented here.

- Gaseous metal vapor is ejected from the capillary during deep-penetration laser welding.
- As the vapor expands and leaves the laser beam caustic, it cools, condenses, oxidizes, and agglomerates into solid particles, which surround the welding zone.
- Some particles drift back into the laser beam, where they are re-heated and potentially reduced, melted, or evaporated.
- Vapor can cool to the evaporation temperature within the caustic, but particle formation is suppressed near the keyhole due to the high beam intensity.
- Up to approximately 35 mm above the welding zone with these laser process parameters, the vapor zone consists mainly of gaseous metal with very few particles.
- Above 125 mm, a particle zone is formed, consisting of liquid and solid material.
- Between these zones lies a multi-phase zone containing both particles and gaseous metal.
- Particles and droplets within the beam caustic scatter and absorb the incident laser beam.
- Dynamic changes of the complex refractive index occur within the beam caustic and can distort the wave front of the incident laser beam.

This qualitative research provides a valid methodology for studying the plume in deep-penetration laser welding. Future work will focus on quantifying laser beam absorption, scattering, and phase front distortion during interactions with the vapor plume and particle cloud. This study enhances our understanding of the fundamental physics of laser welding and will contribute to optimizing welding processes and beam shaping techniques.

Declaration of Generative AI and AI-assisted technologies in the writing process

During the preparation of this work the author used *OpenAI ChatGPT 3.5* and *DeepL Write* in order to improve readability in selected sections. After using these tools, the authors reviewed and edited the content as needed and take full responsibility for the content of the publication.

CRediT authorship contribution statement

Johannes Wahl: Writing – original draft, Visualization, Software, Methodology, Investigation, Formal analysis, Data curation, Conceptualization. **Christian Frey:** Writing – review & editing, Methodology. **John Powell:** Writing – review & editing, Supervision, Methodology. **Felix Zaiß:** Writing – review & editing, Methodology. **Michael Haas:** Writing – review & editing, Methodology. **Simon Olschok:** Writing – review & editing, Funding acquisition. **Uwe Reisgen:** Writing – review & editing, Supervision, Funding acquisition. **Christian Hagenlocher:** Writing – review & editing, Methodology. **Thomas Graf:** Writing – review & editing, Supervision, Methodology, Funding acquisition, Conceptualization.

Declaration of competing interest

The authors declare that they have no known competing financial interests or personal relationships that could have appeared to influence the work reported in this paper.

Acknowledgements

The presented work was funded by the Deutsche Forschungsgemeinschaft (DFG, German Research Foundation) - project number: 463452146. Additionally, we acknowledge partial support from the InnovationCampus Future Mobility funded by the Baden-Württemberg Ministry of Science, Research and the Arts.

Appendix A. Supplementary data

The supplementary data to this publication contains the videos of the schlieren and high-speed images as well as the processed spectral data. https://doi.org/10.18419/darus-3984 [18].

Appendix B. Spectrometer measurements

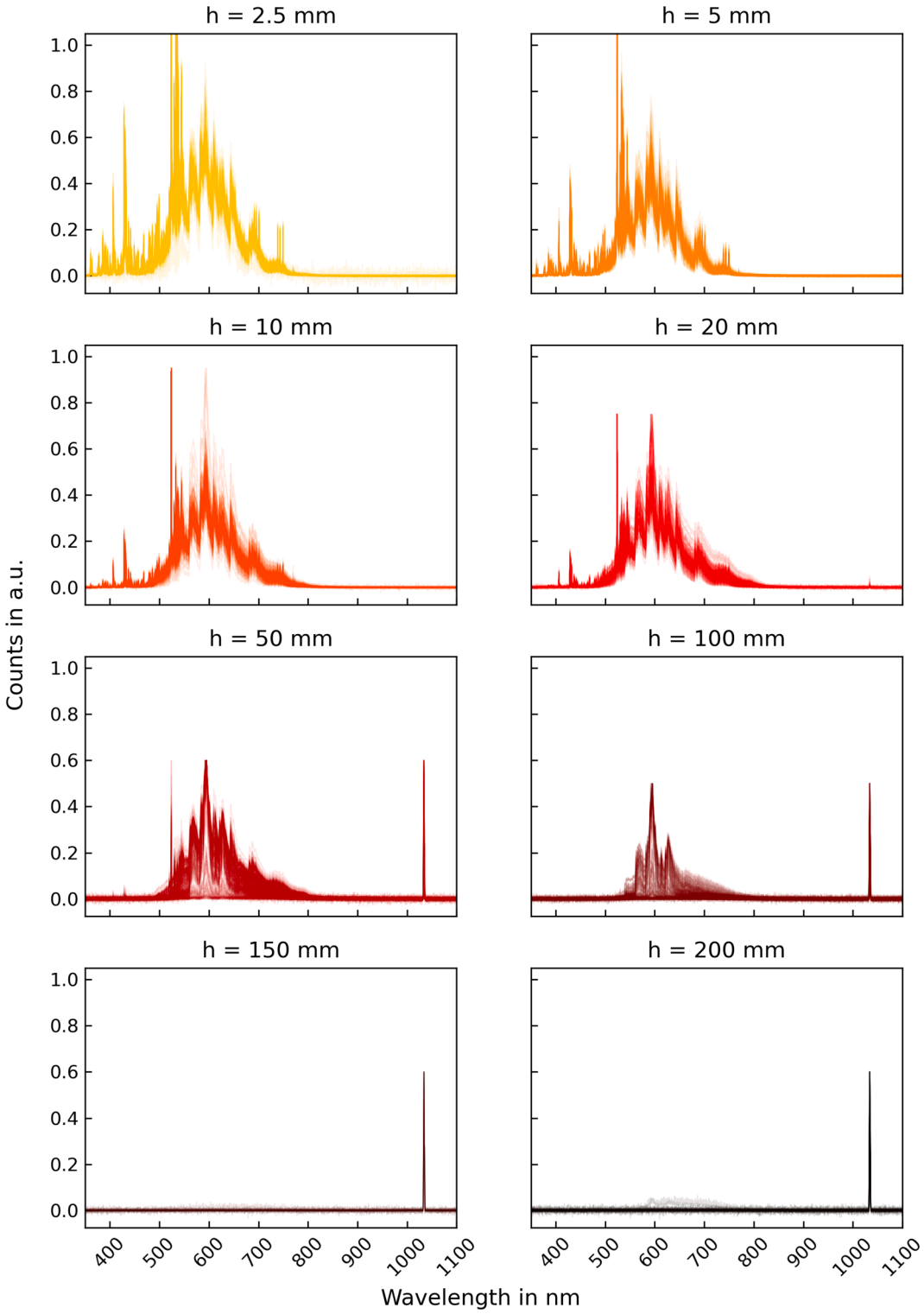


Fig. 14. Captured raw spectra from the vapor plume and particle cloud at different heights above the opening of the keyhole. The individual spectra shown for the same height are 10 ms apart and are plotted with an opacity of 0.1. The relative intensities between the plots are not to scale and have been adapted for better visibility. The spectra data files are available at [18].

Data availability

The data will be availably publicly via a data repository of the University of Stuttgart upon publication.

References

[1] R. Fabbro, M. Hamadou, F. Coste, Metallic vapor ejection effect on melt pool dynamics in deep penetration laser welding, J. Laser Appl. 16 (2004) 16–19, https://doi.org/10.2351/1.1642633.

[2] I. Miyamoto, E. Ohmura, T. Maede, Dynamic behavior of plume and keyhole in CO2 laser welding. In: Proceedings of International Congress on Applications of Lasers and Electro Optics (ICALEO): Laser Materials Processing Conference, 1997, San Diego, CA, USA, November 17th - 20th. Laser Inst. of America (LIA), Orlando, Fla., pp 210–218, 1997.

[3] Y. Kawahito, N. Matsumoto, M. Mizutani, et al., Characterisation of plasma induced during high power fibre laser welding of stainless steel, Sci. Technol. Weld. Join. 13 (2008) 744–748, https://doi.org/10.1179/136217108X329313.

[4] P. Shcheglov, S.A. Uspenskiy, A.V. Gumenyuk, et al., Plume attenuation of laser radiation during high power fiber laser welding, Laser Phys. Lett. 8 (2011) 475–480, https://doi.org/10.1002/lapl.201110010.

[5] A. Michalowski, A. Heß, A. Ruß, et al., Plume attenuation under high power Yb: YAG laser material processing. In: Vollertsen F (ed) Proceedings of Lasers in Manufacturing (LIM): Fourth International WLT-Conference on Lasers in Manufacturing, 2007, Munich, Germany, June 18th - 22nd, 2007. AT-Fachverlag, Stuttgart.

[6] F. Kaufmann, J. Ermer, A. Maier, et al., Influence of plume attenuation under high power laser welding of copper using visible wavelengths, J. Laser Appl. 33 (2021), https://doi.org/10.2351/7.0000505.

[7] A. Mahrle, M. Borkmann, E. Beyer, et al., Efficient air flow control for remote laser beam welding. In: Proceedings of International Congress on Applications of Lasers and Electro Optics (ICALEO): 36th International Congress on Applications of Lasers & Electro-Optics, Vol 30. Laser Inst. of America (LIA), 2017.

[8] J. Zou, W. Yang, S. Wu, et al., Effect of plume on weld penetration during high-power fiber laser welding, J. Laser Appl. 28 (2016), https://doi.org/10.2351/1.4940148.

[9] G.K. Born, R. Bogenberger, K.D. Erben, et al., Phase-front distortion of laser radiation in a turbulent atmosphere, Appl. Opt. (1975) 2857–2863.

[10] A. Brignon (Ed.), Coherent Laser Beam Combining, Wiley-VCH, Weinheim, 2013.

[11] H. Fathi, M. Närhi, R. Gumenyuk, Towards ultimate high-power scaling: coherent beam combining of fiber lasers, Photonics 8 (2021) 566, https://doi.org/10.3390/photonics8120566.

[12] F. Yang, X. Meng, S.N. Putra, et al., Numerical analysis of the effect of an oscillating metal vapor plume on the keyhole and molten pool behavior during deep penetration laser beam welding, J. Laser Appl. 35 (2023), https://doi.org/10.2351/7.0001094.

[13] S. Pang, X. Chen, W. Li, et al., Efficient multiple time scale method for modeling compressible vapor plume dynamics inside transient keyhole during fiber laser welding, Opt. Laser Technol. 77 (2016) 203–214, https://doi.org/10.1016/j.optlastec.2015.09.024.

[14] Y. Kurita, Y. Sato, S. Fujio, et al., Influence of the laser-induced plume on welding behavior in keyhole welding for stainless steel using a 16 kW disk laser, J. Laser Appl. 35 (2023), https://doi.org/10.2351/7.0001173.

[15] J. Greses, P.A. Hilton, C.Y. Barlow, et al., Plume attenuation under high power Nd: yttritium–aluminum–garnet laser welding, J. Laser Appl. 16 (2004) 9–15, https://doi.org/10.2351/1.1642636.

[16] S.A. Uspenskiy, P.Y. Shcheglov, V.N. Petrovskiy, et al., Spectral diagnostics of a vapor-plasma plume produced during welding with a high-power ytterbium fiber laser, Opt Spectrosc 115 (2013) 140–146, https://doi.org/10.1134/S0030400X13070205.

[17] H.G. Taylor, Waldram JM Improvements in the Schlieren method, J. Sci. Instrum. (1933) 378–389.

[18] J. Wahl, Supplementary Data for Paper “Laser-plume interactions in deep-penetration remote laser welding of stainless steel”, 2025. doi: 10.18419/darus-3984.

[19] H.C. de van Hulst, Light scattering by small particles, Unabridged and corrected republication of the work originally published in 1957 by John Wiley & Sons, Inc., N.Y. Dover books on physics. Dover Publications Inc; LSC Communications, New York, 1957.

[20] O. Bocksrocker, P. Berger, S. Kessler, et al., Local Vaporization at the Cut Front at High Laser Cutting Speeds, Lasers Manuf Mater Process 7 (2020) 190–206, https://doi.org/10.1007/s40516-020-00113-3.

[21] M. Schmidt, R. Köhler, C. Gerhard, et al., Laser Cladding With Combined NIR and Blue Diode Laser Including In-Line Atomic Emission Spectroscopy, Lasers Manuf Mater Process 10 (2023) 165–189, https://doi.org/10.1007/s40516-022-00201-6.

[22] J. Powell, D. Petring, R.V. Kumar, et al., Laser–oxygen cutting of mild steel: the thermodynamics of the oxidation reaction, J. Phys. d: Appl. Phys. 42 (2009) 15504, https://doi.org/10.1088/0022-3727/42/1/015504.

[23] A.V. Samrot, C.S. Sahithya, A.J. Selvarani, et al., A review on synthesis, characterization and potential biological applications of superparamagnetic iron oxide nanoparticles, Curr. Res. Green Sustainable Chem. 4 (2021) 100042, https://doi.org/10.1016/j.crgsc.2020.100042.

[24] R. Fabbro, S. Slimani, I. Doudet, et al., Experimental study of the dynamical coupling between the induced vapour plume and the melt pool for Nd–Yag CW laser welding, J. Phys. D: Appl. Phys. 39 (2006) 394–400, https://doi.org/10.1088/0022-3727/39/2/023.

[25] F. Hansen, W.W. Duley, Attenuation of laser radiation by particles during laser materials processing, J. Laser Appl. 6 (1994) 137–143, https://doi.org/10.2351/1.4745348.

[26] T. Scholz, K. Dickmann, A. Ostendorf, Investigation of the formation of nanoparticles during laser remote welding, Phys. Procedia 41 (2013) 90–97, https://doi.org/10.1016/j.phpro.2013.03.055.

[27] P.Y. Shcheglov, A.V. Gumenyuk, I.B. Gornushkin, et al., Vapor–plasma plume investigation during high-power fiber laser welding, Laser Phys. 23 (2013) 16001, https://doi.org/10.1088/1054-660X/23/1/016001.